ELSEVIER

Journal of Structural Geology 28 (2006) 2067–2083

JOURNAL OF STRUCTURAL GEOLOGY

www.elsevier.com/locate/jsg

Basin inversion and fault reactivation in laboratory experiments

Chiara Del Ventisette [a,*], Domenico Montanari [a], Federico Sani [a,b], Marco Bonini [b]

[a] *Dipartimento di Scienze della Terra, Università degli Studi di Firenze, via La Pira 4, 50121 Florence, Italy*
[b] *C.N.R., Istituto di Geoscienze e Georisorse, Sezione di Firenze, via La Pira 4, 50121 Florence, Italy*

Received 5 June 2006; received in revised form 23 June 2006; accepted 7 July 2006
Available online 5 October 2006

Abstract

A series of analogue models have been performed to get insights into the relationships between the reactivation of pre-existing normal faults and the orientation of a successive compressive stress field. The models were deformed in two phases: (1) a first extension phase ($\sigma_h \approx \sigma_3$) generating a graben, and (2) a successive compressive phase with the orientation of the shortening direction ($\sigma_h \approx \sigma_1$) trending between 0° and 90° (obliquity angle α) to the faults bounding the graben. The deepening of this graben was accompanied by syn-tectonic sedimentation that included a basal ductile layer (simulating salt in nature) overlain by a brittle sand pack.

The experimental results suggest that the development of compressive structures is strongly controlled by the pre-existing normal faults and by the obliquity angle α. The experiments have invariably shown that the extensional faults were reactivated during shortening whatever the value of the angle α. Whereas strike-slip reactivation of major normal faults is favoured by low obliquity angles α, mostly dip-slip reactivation of pre-existing structures is instead promoted for high obliquity angles α. The analysis of model results highlights the important role played by a ductile layer at the base of the basin fill, and the obliquity angle α in controlling both strain partitioning and brittle–ductile decoupling.

Keywords: Basin inversion; Fault reactivation; Ductile layers; Analogue modelling

1. Introduction and aim of the work

The final deformation pattern of extensional basins inverted during compression is strongly influenced by the geometry of early normal faults, so that both deformation geometries and the time-space evolution of structures markedly differ from basins related to shortening only. Generally, the early normal faults are zone of weakness with different mechanical properties (cohesion and internal friction) with respect to the surrounding undeformed rocks (Mandl, 1988; Krantz, 1991; Letouzey et al., 1995). Depending on the orientation of the faults relative to the stress field, this variation of mechanical properties along the fault plane may favour its reactivation, since it requires lower differential stresses than those necessary for the development of new structures. However, the complex final deformation pattern of the inverted extensional basins obstacles the progressive restoration of their time-space structural evolution and the recognition of the role of extensional basement structures during fault reactivation. Basement involvement is indeed often hidden by thin-skinned tectonics decoupling the basin fill from the basement along a thick basal layer of salt or other ductile layers.

Fault reactivation and inversion tectonics have been the object of theoretic studies (e.g. Sibson, 1985; Ranalli and Yin, 1990; Yin and Ranalli, 1992; Sandiford, 1999) as well as of analogue and numerical models (Koopman et al., 1987; McClay, 1989; Richard, 1989; Buchanam and McClay, 1991; Richard and Krantz, 1991; McClay and Buchanam, 1992; Sassi et al., 1993; Mitra and Islam, 1994; Mandal and Chattopadhyay, 1995; Letouzey et al., 1995; Nalpas et al., 1995; Brun and Nalpas, 1996; Higgins and Harris, 1997; Dubois et al., 2002; Buiter and Pfiffner, 2003; Hansen and Nielsen, 2003; Panien et al., 2005; Gartrell et al., 2005).

* Corresponding author. Tel.: +39 0552757528.
E-mail address: delventisette@geo.unifi.it (C. Del Ventisette).

0191-8141/$ - see front matter © 2006 Elsevier Ltd. All rights reserved.
doi:10.1016/j.jsg.2006.07.012

The present work intends to examine, by means of an analogue modelling study, the patterns of fault reactivation in relation to the variation of the angle α between pre-existing normal faults bounding a graben and a successive principal compressive stress axis σ_1 ($\sigma_1 \cong \sigma_h$). The analogue modelling technique has been proven to represent a useful tool, as it allows studying the progressive deformation during basin inversion, and may also provide indications about the role of distinct factors controlling the final deformation pattern. Only some previous works focused on fault reactivation associated with oblique shortening (Nalpas and Brun, 1993; Nalpas et al., 1995; Brun and Nalpas, 1996; Dubois et al., 2002; Yamada and McClay, 2003a,b; Gartrell et al., 2005). In particular, Brun and Nalpas (1996) highlighted that the reactivation of border faults need the direction of compression to be less than 45° to the pre-existing normal faults trend. Dubois et al. (2002) instead explored the role of syn-tectonic sedimentation in controlling fault reactivation.

In this work, we have examined in detail how a ductile layer at the base of a syn-rift sequence deposited *within* a graben could affect the deformation pattern during basin inversion, a stratigraphic setting characterising several examples of inverted basins worldwide (e.g. North Sea, Morocco, among the other). Particularly, we have focused our study on the structural styles resulting from the shortening of a syn-rift sequence produced by a principal stress σ_1 oblique to the graben axis, including graben-parallel and graben-orthogonal shortening end-members.

2. Analogue modelling

The models simulated – at a first approximation – the geological setting observed in some natural cases characterized by the reactivation of faults bounding a graben containing a salt layer at the base of the syn-rift sequence. In our models the salt layer is restricted to the base of the graben, and does not extend over the graben shoulders as in previous models (e.g. Nalpas and Brun, 1993; Brun and Nalpas, 1996; Gartrell et al., 2005). For scaling of time and thickness of syn-tectonic sedimentation we used the data of some Moroccan basins (Meknes-Fes Basin and Essaouira Basin; Faugères, 1978,1981; Zizi, 1996a,b; Piqué et al., 1998; Hafid, 2000; Hafid et al., 2000; Bouatmani et al., 2003).

2.1. Model construction and deformation

Analogue models were performed in a pure-shear/simple-shear deformational apparatus (Fig. 1) settled at the Tectonic Modelling Lab of CNR-IGG at the Department of Earth Sciences in Florence. Models were geometrically and dynamically scaled to nature (for model scaling, see Appendix A). Each model was deformed through two successive deformation phases, a first orthogonal extension followed by a phase of shortening. The first extensional phase was identical in all experiments in terms of bulk extension and velocity. This phase also simulated the syn-rift sedimentation represented by a basal ductile salt layer overlain by a brittle syn-rift sequence. During

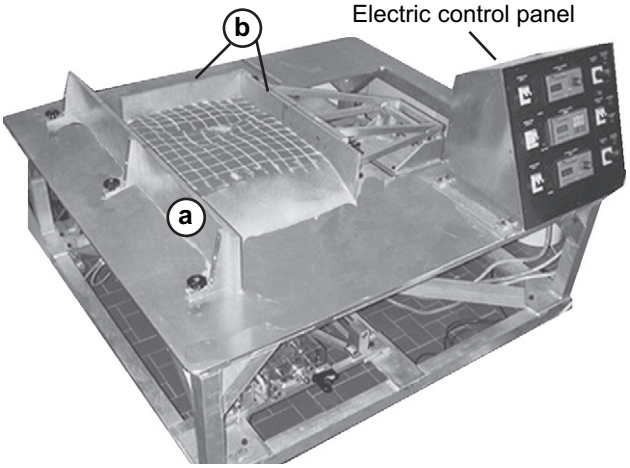

Fig. 1. Experimental apparatus of pure-shear/simple-shear deformation consisting of a fixed wall (a) and two moving walls (b) connected to electric motors. These latter are controlled by an electric control panel, which allows imposing the velocities to the moving walls, and thus to obtain the requested orientation of shortening.

the latter deformation phase, the models were shortened with different angles α, the angle between the direction of the maximum horizontal stress axis (σ_1) and the trend of the main normal faults related to the first-phase graben. This angle α was varied between 0° and 90° (Fig. 2a; Table 1).

In previous analogue modelling studies, the models were normally built above a rigid basal plate creating a basal velocity discontinuity (VD) during the extension phase (e.g. Nalpas and Brun, 1993; Fig. 2a). However, such a basal plate also produces a strong localization of deformation during the phase of shortening, which may thus potentially influence the reactivation of pre-existing faults. In order to minimize these effects, in our experimental set-up the metal plate was replaced by an acetate sheet, which was fixed to the moving wall in a way that it could be easily deactivated during the second deformation phase. This technical solution allowed to distribute shortening, and thus to prevent the development of strain localization arising from a rigid basal plate. During the extension phase, the basal VD induced the nucleation of normal faults bounding a roughly symmetric graben surfacing in the central part of the model, as observed in several previous studies (e.g. Allemand et al., 1989; Tron and Brun, 1991; Brun and Nalpas, 1996).

A 1 cm-thick layer of Mastic Rebondissante 29 silicone putty was laid above the basal acetate sheet and this contributed to considerably reduce the control exerted by the VD on the development of normal faults. In order to appreciate the strike-slip reactivation of the earlier extensional basement normal faults during the successive compressive phase, 3.5 cm-wide coloured sand bands were placed into the model basement parallel to the extension direction (indicated as Coloured Marker Layer, CML in Fig. 2b, c). A change in colour in the CML layer close to a reactivated basement fault thus allowed the detection of strike-slip reactivation components.

The models were extended at a constant velocity of 10 mm/h for 7 h up to a bulk extension (BE) of about 16.5%. After 2 h 30′ of deformation (approximately 5.7% BE), the graben was

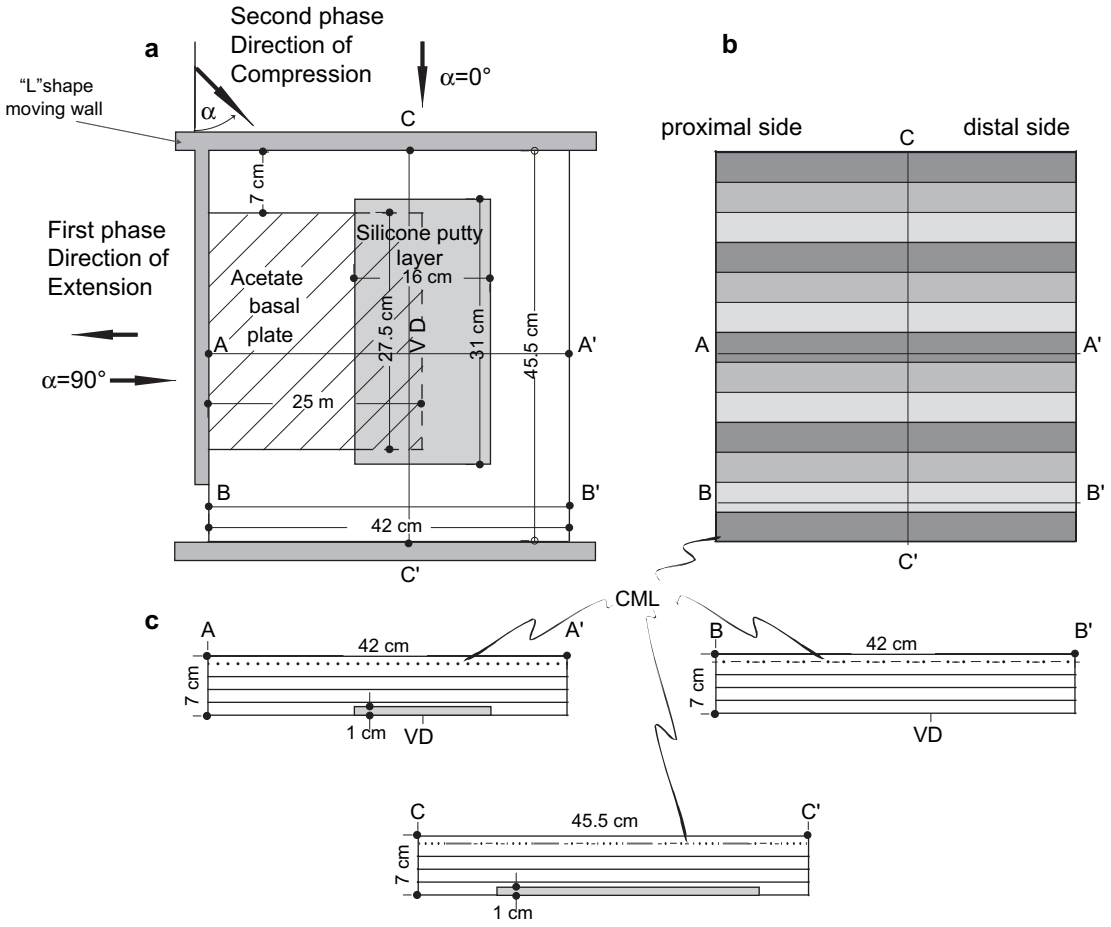

Fig. 2. Initial model set-up: (a) plan view of initial model set-up illustrating the position of the basal acetate plate and the basal silicone layer; VD = velocity discontinuity. (b) The uppermost coloured layer (CML) consists of bands -approximately 3.5 cm wide- of differently coloured sand (see text for detail); (c) cross-sections of the initial model set-up in different sectors of the model.

ca. 1 cm deep and 1 cm-thick layer of silicone and oleic acid was placed at the base of the graben to simulate the deposition of a basal syn-rift salt layer. The successive syn-tectonic sedimentation consisted of dry quartz-sand layers, with different colours, sieved at regular time intervals. The final thickness of sediments inside the graben was of the order of 3 cm, which represent about 3 km in nature (Table 2). At the end of this phase, a thin black layer of dry sand was sieved on the model surface. A grid of passive markers was drawn onto the model surface to evidence the faults offset, and to estimate the horizontal displacement vectors during the following shortening phase.

The second-phase lateral shortening was applied pushing the "L" shape moving wall, at the constant velocity of 10 mm/h for 7 h, producing a shortening of 7 cm along shortening vector (Fig. 2a). During model deformation, top view photographs were taken at regular time intervals for studying the time-space evolution of structures. At the end of the experiments, dry sand was sieved on the model surface to preserve the final topography. Then, models were wetted with water and serial cross-sections were cut perpendicular to the graben axis approximately every 2 cm for reconstructing the three-dimensional final deformation pattern.

2.2. Analogue materials

The models had initial dimensions of 45.5 cm × 42 cm × 7 cm and consisted of a multi-layered system representing

Table 1
Analogue models performed

Models	EV (mm h^{-1})	Amount of extension (h)	(α) (degrees)	SV (mm h^{-1})	Amount of shortening (h)
Mor-00	10	7	–	–	–
Mor-01[a]	10	7	0	10	7
Mor-02	10	7	10	10	7
Mor-03	10	7	30	10	7
Mor-04[b]	10	7	50	10	7
Mor-05	10	7	20	10	7
Mor-06	10	7	70	10	7
Mor-07	10	7	90	10	7
Mor-08	10	7	10	10	7
Mor-09[a]	10	7	0	10	7
Mor-10[b]	10	7	50	10	7

[a] Models deformed whit same boundary condition but whit and without the silicone layer on VD.

[b] Models deformed with same boundary condition but whit and without the silicone layer at the base of sin-rift sequence. EV = extension velocity; SV = shortening velocity.

Table 2
Analogue modelling parameters[a]

Parameter	Model	Nature	Model/ nature ratio
BL density, ρ_{bsk}(kg m^{-3})	1300	2600	0.5
BL friction coefficient, μ_{bsk}	≈0.8		
DL (Salt) density, ρ_{dsk} (kg m^{-3})	1060	2200	≈0.5
DL (Salt) viscosity, η_{dsk} (Pa s)	10^3	5×10^{17}	2×10^{-15}
Scaling parameters			
Strain rate, ε (s^{-1}) $\varepsilon^* = \sigma^*/\eta^*$			3.4×10^9
Gravity acceleration, g (m s^{-2})	9.81	9.81	1
Length, l (m)	0.01	1000	1×10^{-5}
Stress, σ (Pa) $\sigma^* = \rho^* g^* l^*$			4.8×10^{-6}
Time, t (s) $t^* = 1/\varepsilon^*$	3600	1.3×10^{13} (≈0.4 Ma)	$\approx 2.8 \times 10^{-10}$
Rate of displacement, v (m s^{-1}) $v^* = \varepsilon^* l^*$	2.7×10^{-6}	7.9×10^{-11} (2.5 mm y^{-1})	3.4×10^4
Syn-tectonic sedimentation rate, (m s^{-1})	5.5×10^{-7}	1.6×10^{-11} (0.58 mm y^{-1})	3.4×10^4

[a] The asterisk indicates the ratio between the model and the natural prototype. Abbreviation are as follows: BL, brittle layer; DL, ductile layer. For scaling detail and rheology of materials see the text.

the crystalline basement of a natural prototype (e.g. Nalpas and Brun, 1993; Fig. 2). The brittle behaviour of rocks (basement and upper syn-rift sequence) was simulated by Fontainebleau dry quartz-sand, with grain dimension lower than 250 μm. Our laboratory measurements indicate a cohesion $c \approx 66$ Pa and coefficient of friction $\mu \approx 0.84$ ($\phi \approx 40°$; for materials properties, see also Table 2), which is in agreement with the μ value of natural rocks (0.6–0.85; Byerlee, 1978; Brace and Kohlmmstedt, 1980). The Mastic Rebondissante 29 silicone putty (produced by CRC Industry, France) placed at the base of the model has density (ρ) of kg/m^3 and a Newtonian behaviour with dynamic viscosity Pa s (Table 2). The ductile behaviour of the salt-simulating décollement at the base of the graben was instead simulated by a mixture of silicone Mastic Rebondissante 29 and oleic acid with proportions 4:1 (in weight). This mixture has a density (ρ) of 1060 kg/m^3 and exhibits a Newtonian behaviour with dynamic viscosity $\approx 10^3$ Pa s (see Table 2).

3. Results of modelling

The experimental results are discussed below starting from the extensional phase, and then it continues showing the variation in deformation pattern resulting from the successive compressive phase. For comparison, a model without the silicone layer at the base of syn-rift sequences is also shown to evidence the role of ductile layers on basin inversion.

3.1. The extension phase

To compare the effect of shortening on previous structures, a test model (model Mor-00) was deformed only in extension with bulk extension (BE) and strain rate equal to those applied to the other two-phase models. Top view photographs (Fig. 3a) evidence the development of extensional structures similar to those observed at the end of the extensional phase in the other models. The deformation pattern of model Mor-00 is characterized by a single graben delimited by two transtensional shear bands acting as transfer zones that developed in correspondence of the upper and lower transversal boundaries of the basal acetate plate (Figs. 2 and 3a).

Although in top view the graben is characterized by a quite symmetric geometry, in cross-sections it shows a substantial internal asymmetry. The syn-rift sequence inside the graben shows two opposed wedge trends due to the different activation in time of the normal faults (for a detailed discussion, see Del Ventisette et al., 2005). The graben attains a maximum depth of ca. 4 cm, and is composed of six main faults, two of them dipping towards the right-hand side and four dipping towards the left-hand side (Fig. 3b). The upper segment of the faults is characterized by a minor dip angle, probably because of the local and progressive back stepping of sand due to gravity sliding (Mandl, 1988; Faccenna et al., 1995).

3.2. The shortening phase

Seven analogue models investigated various angles α ranging from 0° to 90° ($\alpha = 0°$, 10°, 20°, 30°, 50°, 70° and 90°; Table 1). Fig. 4 shows the models results, particularly the different deformation patterns (in map view) in the various models at different times of deformation (after 2, 4, 6 and 7 h of deformation, respectively). Fig. 5 illustrates some close-up of model cross-sections representative of the most relevant deformation features.

3.2.1. Shortening perpendicular to the graben axis (Model Mor-07, $\alpha = 90°$)

The comparison between the top view photographs at the end of the first deformation phase with those at the end of shortening shows that deformation is almost exclusively localized along the pre-existing structures. The final deformation pattern is characterized by reverse faults typically developed perpendicularly to the direction of shortening (Fig. 6a). No evidence of strike-slip movements along the early normal faults are observed from the passive grid, whereas inversion with horizontal throw of few millimetres characterizes instead the early shear zones oriented nearly 30° to the direction of compression (faults drawn in halftone in Fig. 6a). The central part of the graben is characterized by a 20 cm long thrust anticline showing a minor crestal graben (Figs. 5g and 6a).

Important dip-slip reactivations along pre-existing faults are clearly illustrated by the deformation of the top view grid (Fig. 6) and model cross-sections (Figs. 5g and 6b). Deformation appears to be concentrated within the model "basement", whereas deformation in the graben fill is mainly accommodated by thrust décollement with top-to-the-left

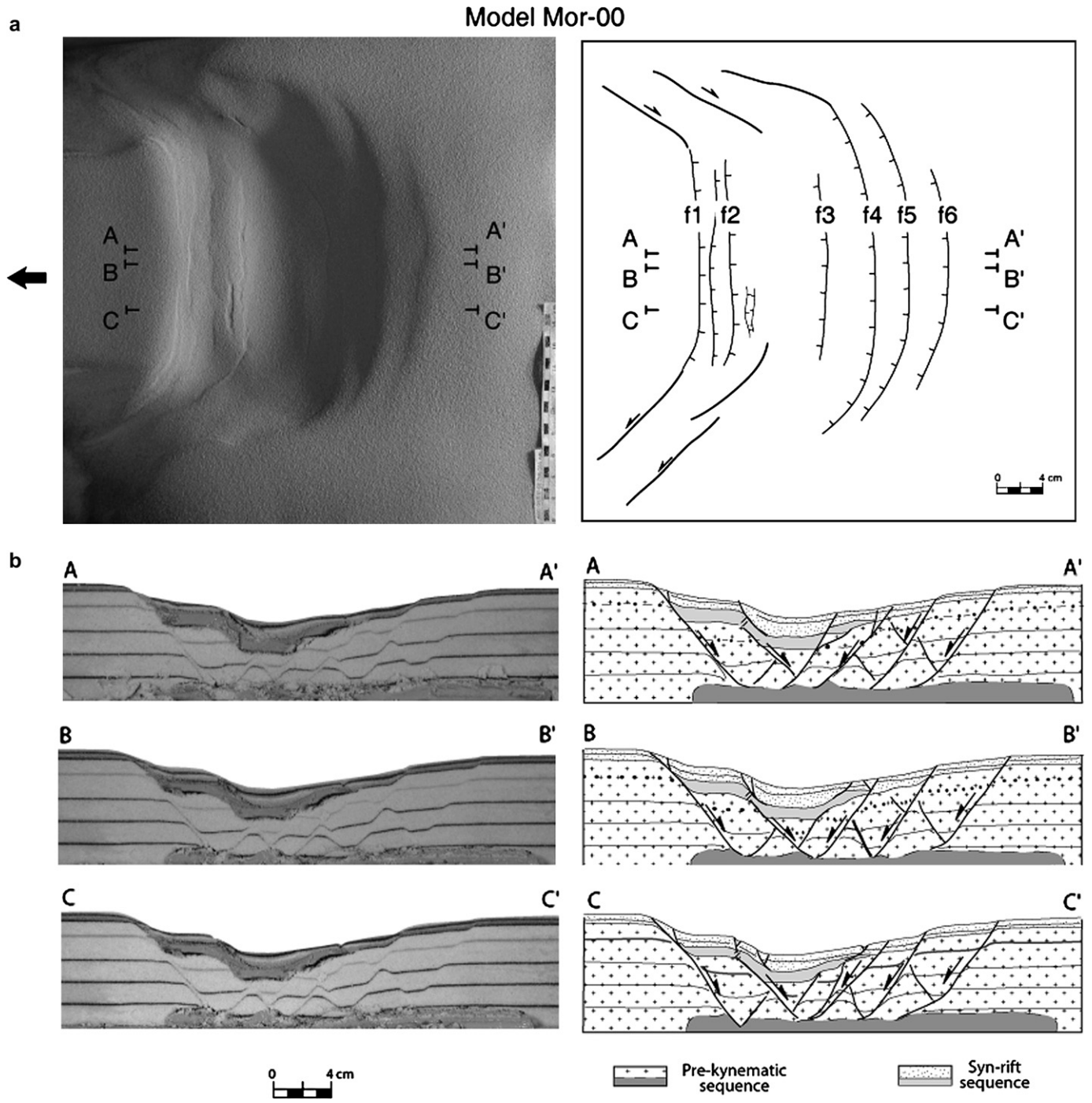

Fig. 3. (a) Top view photograph and line drawing of model Mor-00, deformed only in extension, at the end of deformation; (b) cross-sections photos (left) and line drawings (right) of the model Mor-00 at the end of deformation (location of cross-section in (a)). Basal and syn-kinematic silicone putty layers are indicated in halftone patterns.

movement that is clearly controlled by the silicone layer (Fig. 6b). This structure exhibits a flat-ramp geometry in which the flat is localized at the basement–ductile layer interface, while the ramp reactivates the upper portion of a pre-existing normal fault. Moreover, to the anticline structure is associated with a well-developed ''intrusive diapir'' (Fig. 6b; section A–A′) developed during shortening because of the strong dip-slip reactivation underwent by the underlain early normal fault (Del Ventisette et al., 2005).

In cross-sections, the CML in the basement did not evidence any variation in colour across basement faults, demonstrating the lack of any relevant strike-slip reactivation of pre-existing normal faults. In essence, when the graben is shortened perpendicularly to its longer axis, deformation is

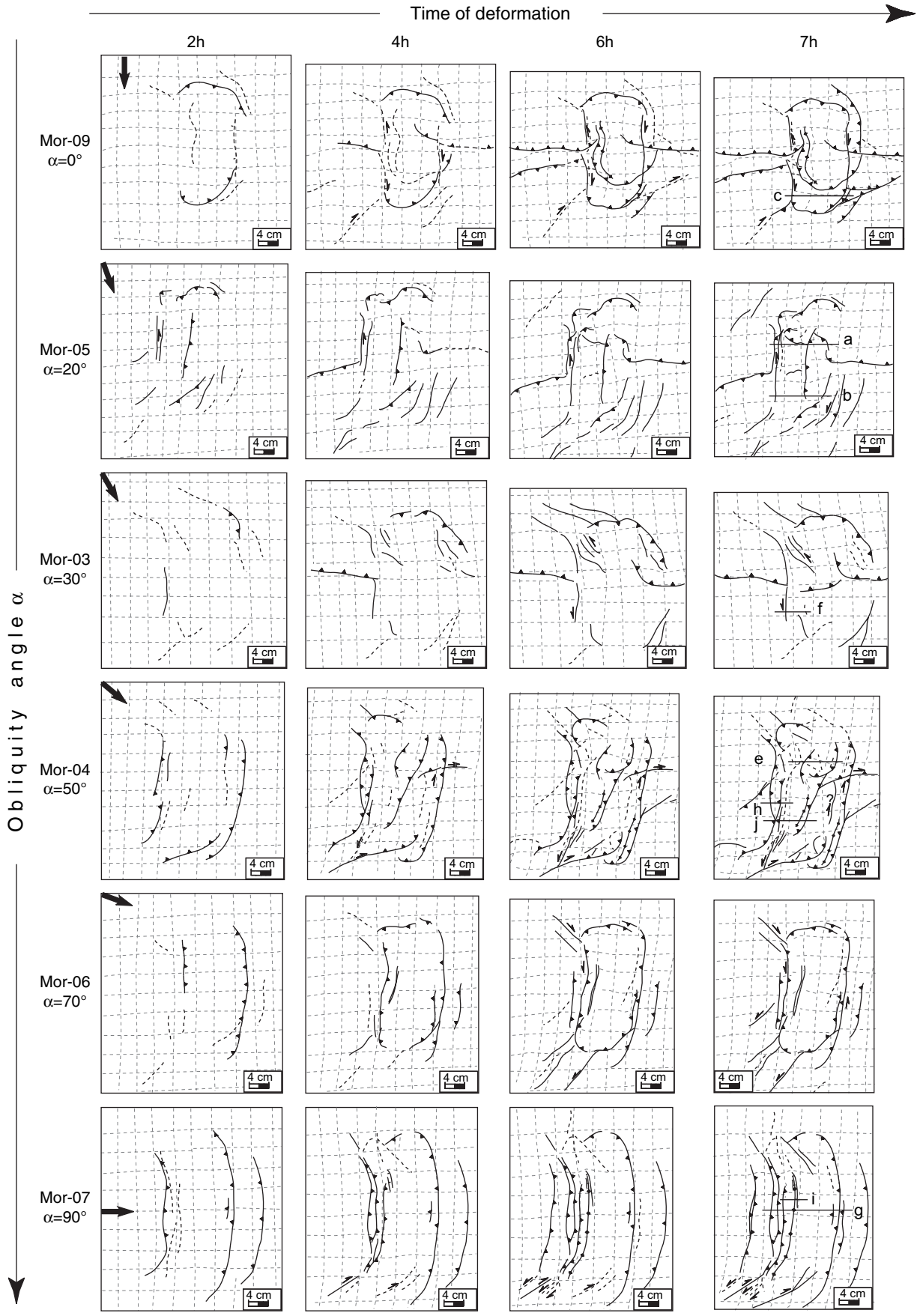

Fig. 4. Line drawings of top view of all the models at different times of deformation. The obliquity angles α (0°, 20°, 30°, 50°, 70°, and 90°) increases along the *Y* axes, while the time of deformation (after 2, 4, 6 and 7 h, respectively) increases along the *X* axes. (a–j) trace of cross-sections shown in Fig. 5.

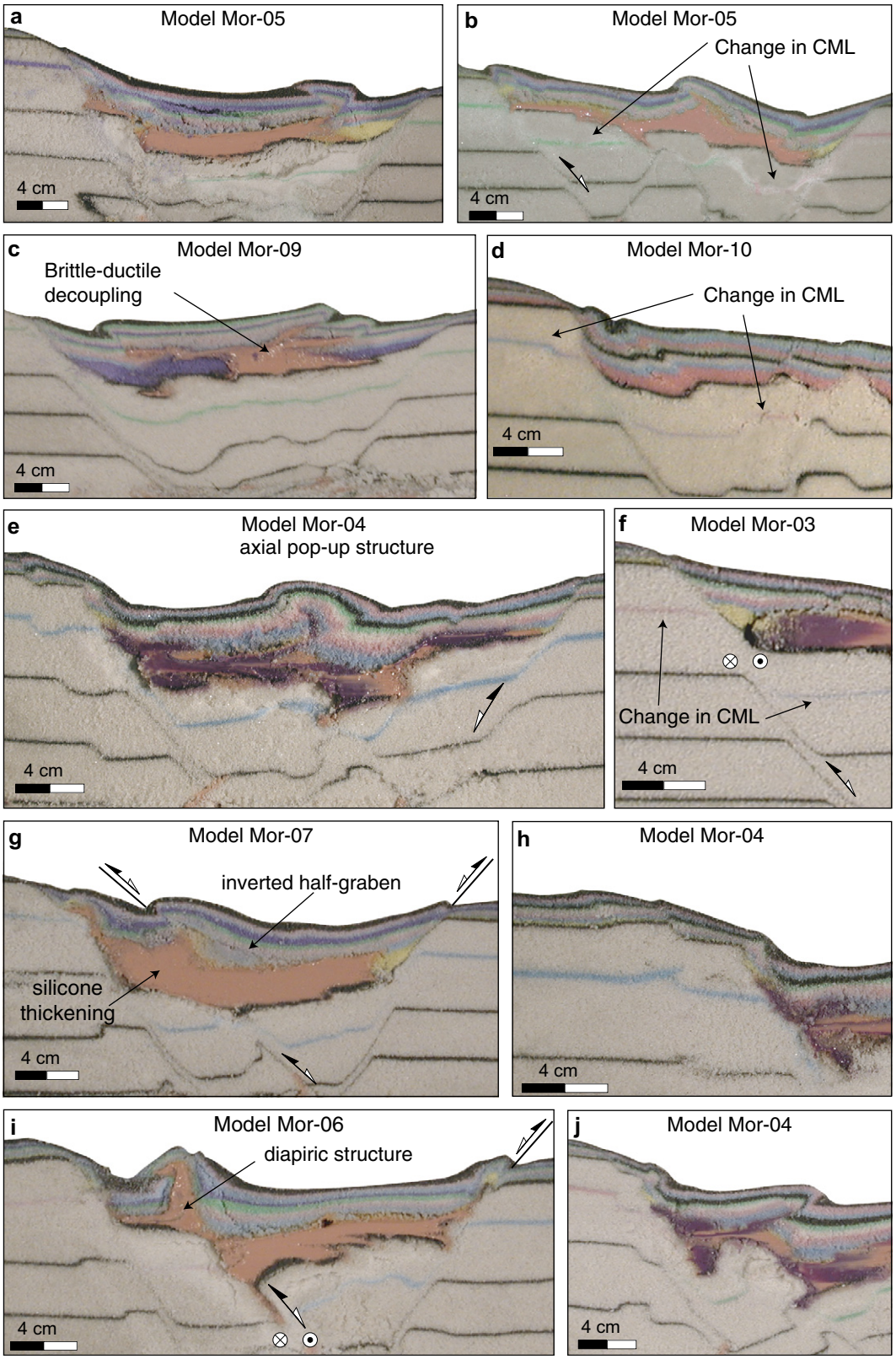

Fig. 5. Close-up of some structural features of models. (a–b) change of colours in CML in model Mor-05 ($\alpha = 20°$) highlighting strike-slip reactivation of basement faults; (c) example of thin-skin-tectonics with decoupling between basement and sedimentary cover in the model Mor-09 ($\alpha = 0°$); (d) example of change colours in CML in the model Mor-10 ($\alpha = 50°$) without syn-rift silicone putty; (e) doubly-vergent structure with rise of silicone in the model Mor-04 ($\alpha = 50°$); (f) example of colours change in CML in the model Mor-03 ($\alpha = 30°$); (g) example of inversion of the external fault in the model Mor-07 ($\alpha = 90°$); (h) example of interference between reactivated early normal fault and new-forming thrust fault in the model Mor-04 ($\alpha = 50°$); (i) example of strong fault reactivation in the model Mor-06 ($\alpha = 70°$); (j) example of strong reactivation of internal faults (both in strike-slip and dip-slip mode) in the model Mor-04 ($\alpha = 50°$).

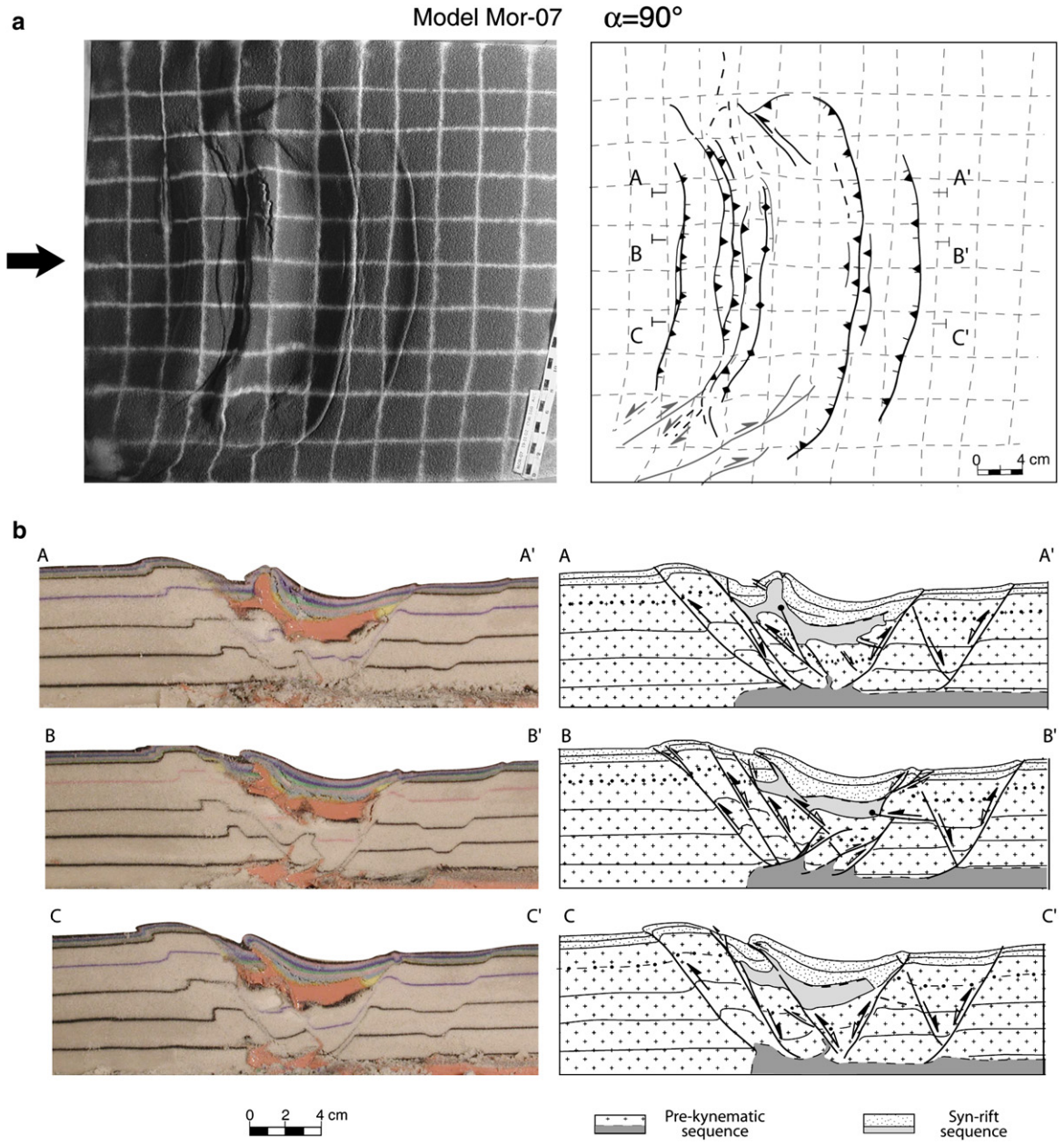

Fig. 6. (a) Top view photograph and line drawing of model Mor-07 ($\alpha = 90°$) at the end of the shortening phase; (b) longitudinal cross-sections and line drawing of model Mor-07 ($\alpha = 90°$). The silicone layers are marked with halftone patterns. Location of cross-sections is indicated in Fig. 6.

mainly accommodated by the dip-slip reactivation of pre-existing extensional structures, both in the basement and in the basin fill without the development of relevant newly-formed structures.

3.2.2. Shortening parallel to the graben axis (Model Mor-09, $\alpha = 0°$)

The surficial fault pattern is characterized by two main thrust-décollements, trending orthogonal to the graben axis and developed at the lateral termination of the graben (Fig. 7a). These structures accommodate the marked decoupling of the basin fill from the basement. A major newly-formed thrust fault, striking orthogonal to the direction of compression, cuts across the whole model. This structure is well-developed on the graben shoulders, while its propagation into the basin is more complex, as it interferes with both pre-existing normal faults reactivated as tear-faults and with newly-formed structures emanating from the syn-rift ductile layer at the base of the graben fill. In cross-section, the pre-existing normal faults are generally reactivated prevalently with strike-slip components, as displayed by the change in colour of the CML across the basement fault planes (Fig. 7b; section A−A′) and, at surface, by the passive grid deformation.

Despite the graben was shortened parallel to its axis, some sectors of the border faults display a minor dip-slip component of reactivation (Fig. 7a). This fault reactivation can be probably related to a local stress reorientation in correspondence of the fault plane or, alternatively, to the rotation of the faults or

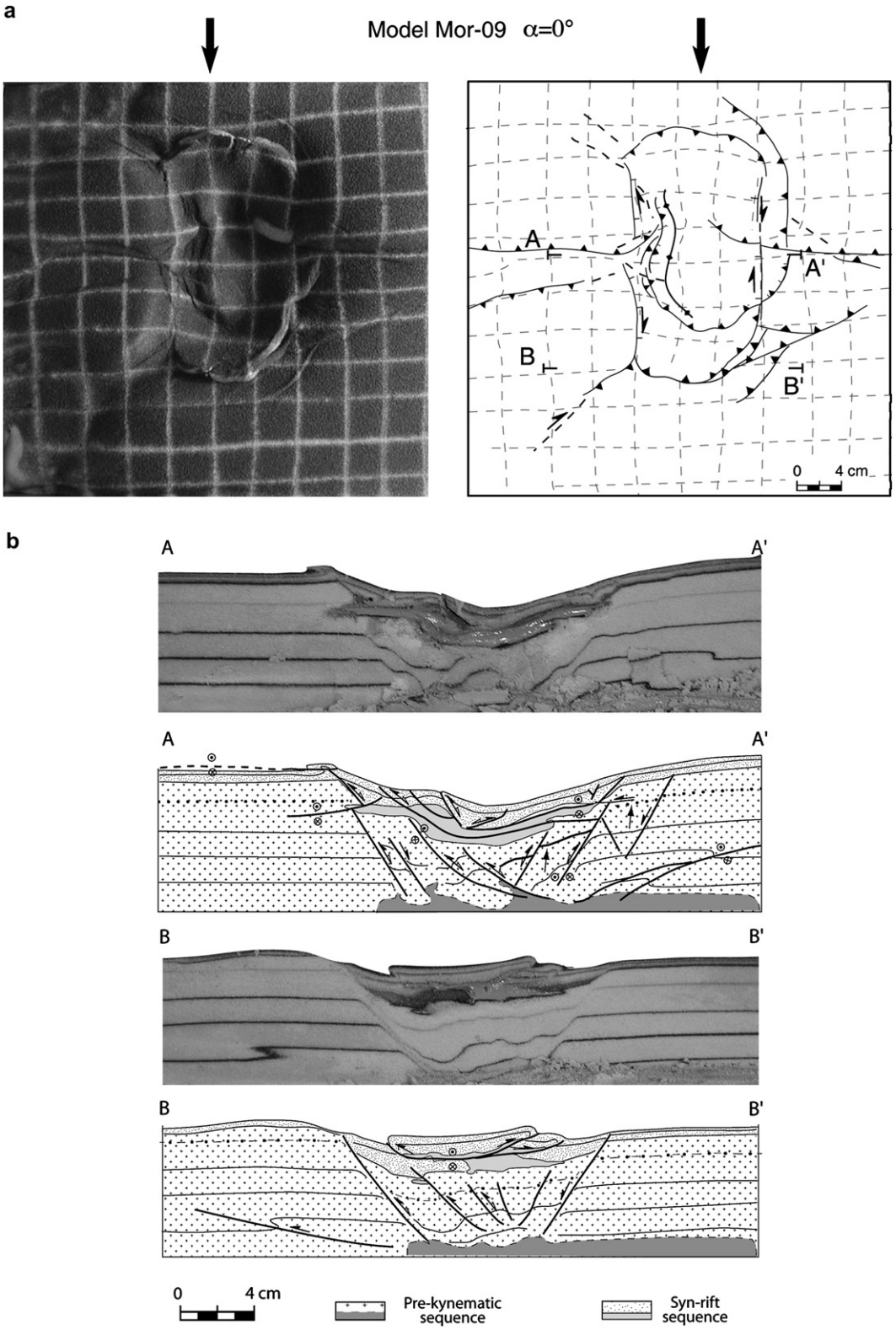

Fig. 7. (a) Top view photo and line drawing at the end of the second (shortening) deformational phase of the model Mor-09 ($\alpha = 0°$); (b) longitudinal cross-sections and line drawings (location in a). Note the change in colour of CML in section A–A′ marked by halftone arrows.

some of their portion relative to the stress field. The basement faults show also a dip-slip component of reactivation at least for the uppermost segment of the fault bounding the syn-tectonic basin fill (Fig. 7a, b). Thin-skinned tectonics in the graben lead to the doubling of the basin fill along the syn-tectonic ductile layer (Fig. 5c).

The comparison of model cross-sections with top view photographs shows that the reactivation of structures on

model surface is not necessarily directly related to movement of basement faults. Particularly, it is worth noting that the passive grid dislocation in correspondence of the most external reactivated normal faults indicates a left lateral movement (Fig. 7a), while the CML across a basement fault indicate a right-lateral movement (Fig. 7b, section A–A′). These opposite directions of movement are likely controlled by the silicone layer at the base of basin fill that – at the model strain rate – strongly decouples the basin fill from the basement.

3.2.3. Shortening oblique to the graben axis ($\alpha = 10°, 20°, 30°, 50°, 70°$)

The models with shortening oblique to the graben axis exhibit a gradual transition of the deformation pattern between the two previously described end-members ($\alpha = 0°$ and $\alpha = 90°$). The transition (highlighted in Fig. 4) may be, however, sub-divided into two main groups characterized by the common features (low obliquity angles vs. high obliquity angles).

For low obliquity angles ($\alpha = 10°$, 20° and 30°) the final deformation patterns are characterized by the strong strike-slip reactivation of the graben border faults and by the presence of main thrust faults with variable strikes in relation to the obliquity angle. In these models, the graben faults generally act as tear-faults. Cross-sections demonstrate that the strike-slip reactivation of the early normal faults affects also the basement sequence, as demonstrated by the CML colour change observed, for instance, in model Mor-03 ($\alpha = 30°$; Fig. 5f) and in model Mor-05 ($\alpha = 20°$; Fig. 5d).

The intermediate top views of these models show that minor thrusts- and back-thrusts are emanated from the syn-rift ductile layer in correspondence of rheological discontinuities at the upper and lower margins of the graben. This results in a typical along-axis ‘‘pseudo-extrusion’’ of the graben fill, which is accommodated by lateral ramps reactivating in strike-slip mode the upper part of the graben border faults.

With increasing α, the model Mor-04 (shortened at $\alpha = 50°$) shows that deformation is characterized by thrusting mostly developed obliquely to the maximum stress axis (Figs. 4 and 8). As in the previous models, the lower part of the basin appears ‘‘extruded’’ and the early normal faults are reactivated. Comparing final top view and cross-sections, the strike-slip reactivation appears less developed in sedimentary cover than in the basement. Whereas the passive grid on top of the model shows a very little dislocation, the juxtaposition of the different colours of the CLM level (testifying strike-slip reactivation) are clearly evident in cross-sections (Fig. 8). An example of the very complex structural pattern is illustrated by a 3D reconstruction (Fig. 9). The central part of the graben is characterized by a doubly-vergent structure with a pop-up-like geometry, in which silicone rises at its core (Figs. 5 and 9). This geometry of deformation may be related either to a change of the vergence of this structure during deformation, or to the reactivation of a pre-existing (first-phase) discontinuity with synchronous development of the double-vergence.

For $\alpha = 70°$ (Model Mor-06), the final deformation pattern is characterized by a localization of deformation in correspondence of the graben border faults (Fig. 4). Away from these reactivated normal faults, no evident deformation is recognizable. The early normal faults are characterized by a prevalent dip-slip reactivation, as clearly shown by the transversal cross-sections (Fig. 5i).

Notably, the reactivation of the internal graben fault in the models with high obliquity angles ($\alpha = 50°$ and 70°; model Mor-04 and Mor-06, respectively) led to the formation of a ‘‘salt’’ wall similarly to what observed in model Mor-07 ($\alpha = 90°$), where shortening was applied perpendicularly to the graben axis (Fig. 6a and b).

3.2.4. Model without ductile layer at the base of graben fill (Model Mor-10, $\alpha = 50°$)

The final surface deformation pattern of model Mor-10 was strongly different from the correspondent model performed with the silicone putty layer (i.e. model Mor-04; cf. Fig. 8 with Fig. 10). The comparison of cross-sections of model Mor-10 with those of modes built with silicone at the base of the graben fill evidences the very different deformation patterns exhibited by the sedimentary cover (compare Figs. 8 and 9 with Fig. 10). The most important difference is that the structures related to the ‘‘pseudo-extrusion’’ along the graben observed in the model with syn-rift silicone layer are instead, as expected, lacking in model Mor-10. Rather, top view photographs reveal that model Mor-10 is affected by major oblique thrusts roughly orthogonal to the maximum stress axis. This model emphasizes once more the importance of ductile layer in decoupling large section of the sedimentary cover, as well as in localising and controlling the deformation patterns.

3.3. Analysis of model results

3.3.1. Fault dip and rotation during graben inversion

At the end of deformation, dip angles of the major faults have been measured on cross-sections taken in the central part of the models to avoid border effects. The upper part of the faults was not considered because of the local back stepping due to the sand dilatancy coming near surface and to little gravity motions (e.g. Mandl, 1988; Faccenna et al., 1995). To better constrain the dip value, we have averaged these data on four cross-sections. Fig. 11b shows the dip angles for the considered faults depending on angles α. Since the extensional phase is the same for each model, the variations in the amount of rotation for each model has been assumed to be directly related to the obliquity angle α of the second deformation phase. The variation of the dip angle illustrated in Fig. 11c was calculated in relation to the mean dip value of the faults measured at the end of the extensional phase in model Mor-00 (see Section 4). The faults invariably underwent a clock-wise rotation. In particular, faults f_1 and f_2 (Fig. 11a, c) show an increase of dip angle with increasing angle α (with a maximum rotation of about 7.5° for f_1 and 4.5° for f_2, respectively), while the most external faults f_5 and f_6 show a decrease

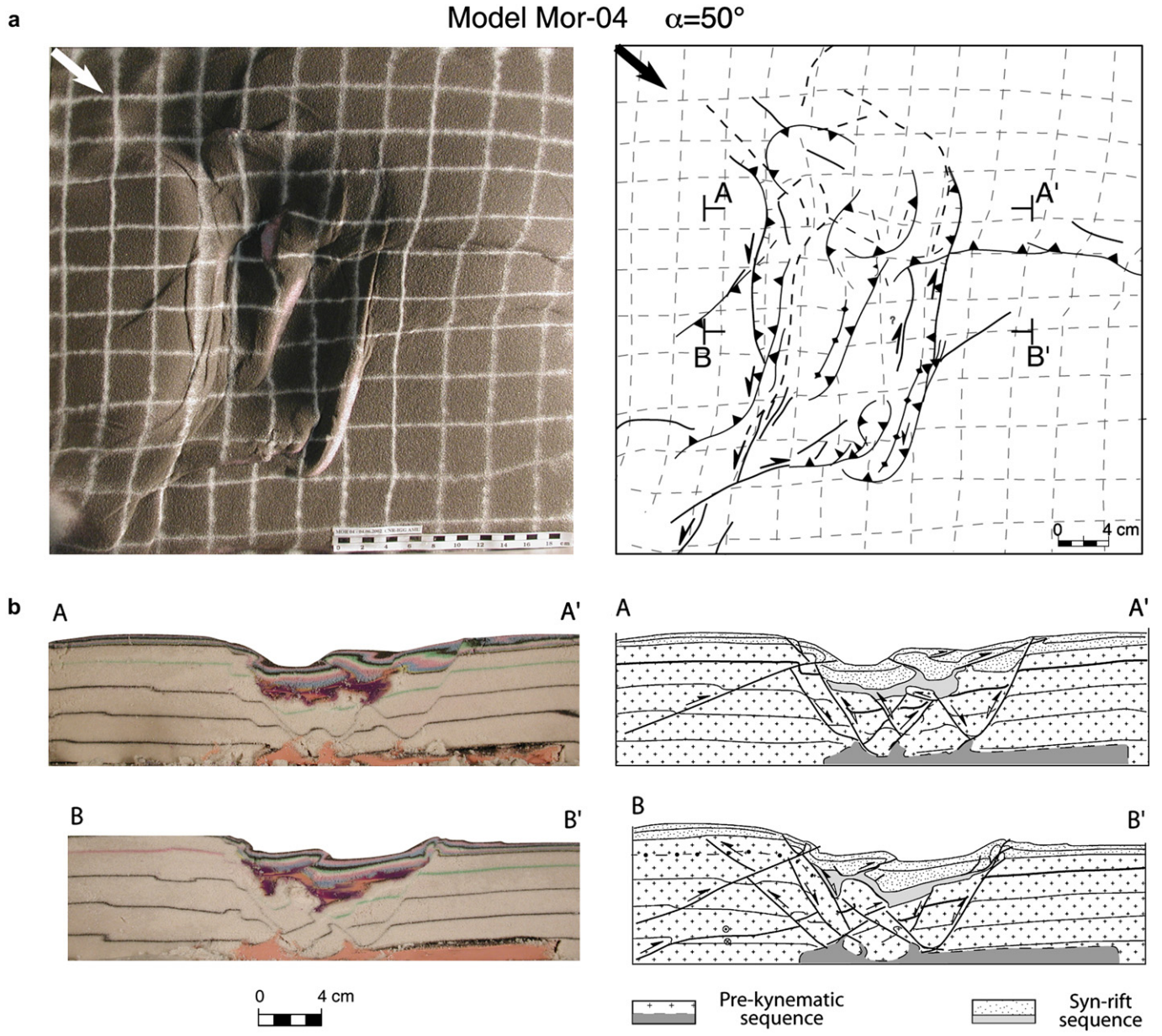

Fig. 8. (a) Top view photo and line drawing at the end of the shortening phase of model Mor-04 ($\alpha = 50^\circ$); (b) longitudinal cross-sections and line drawing (location in (a)).

of the dip angle with increasing the obliquity angle α (about 3° and 2° for f_5 and f_6, respectively, at $\alpha = 90^\circ$). Best fitting indicates that the dip rotation is illustrated by a linear relation proportional to α and inversely proportional to the distance from the moving wall (Fig. 11). The most internal faults f_1 and f_2 exhibit indeed rotational values comparatively higher with respect to the most external faults (f_5 and f_6; Fig. 11c). To explain the different dip rotation, we may consider two hypotheses. In the first, the dip rotation could be the result of differential horizontal sand compaction during shortening. In the second hypothesis, rotation can occur because of the reorientation of fault planes before or during their reactivation. Given that rotations have been observed also during experiments performed with two oblique extensional phases (e.g. without shortening; Dubois et al., 2002), it is possible to argue that the compaction of sand during shortening cannot be invoked as the only cause responsible for the rotation of fault planes.

3.3.2. Graben width vs. angle α

Variation of graben width in relation to angle α is plotted in Fig. 12a. For each model, the graben width has been calculated as the average value of the base of the syn-rift silicone measured in four cross-sections (Fig. 12b). The best fit-curve better approximating the graben width variations is a binomial curve (Fig. 12a). This curve outlines two different linear trends intercepting at $\alpha \approx 40^\circ$. This subdivision evidences that $\alpha = 40^\circ$ represents a critical value separating two distinct

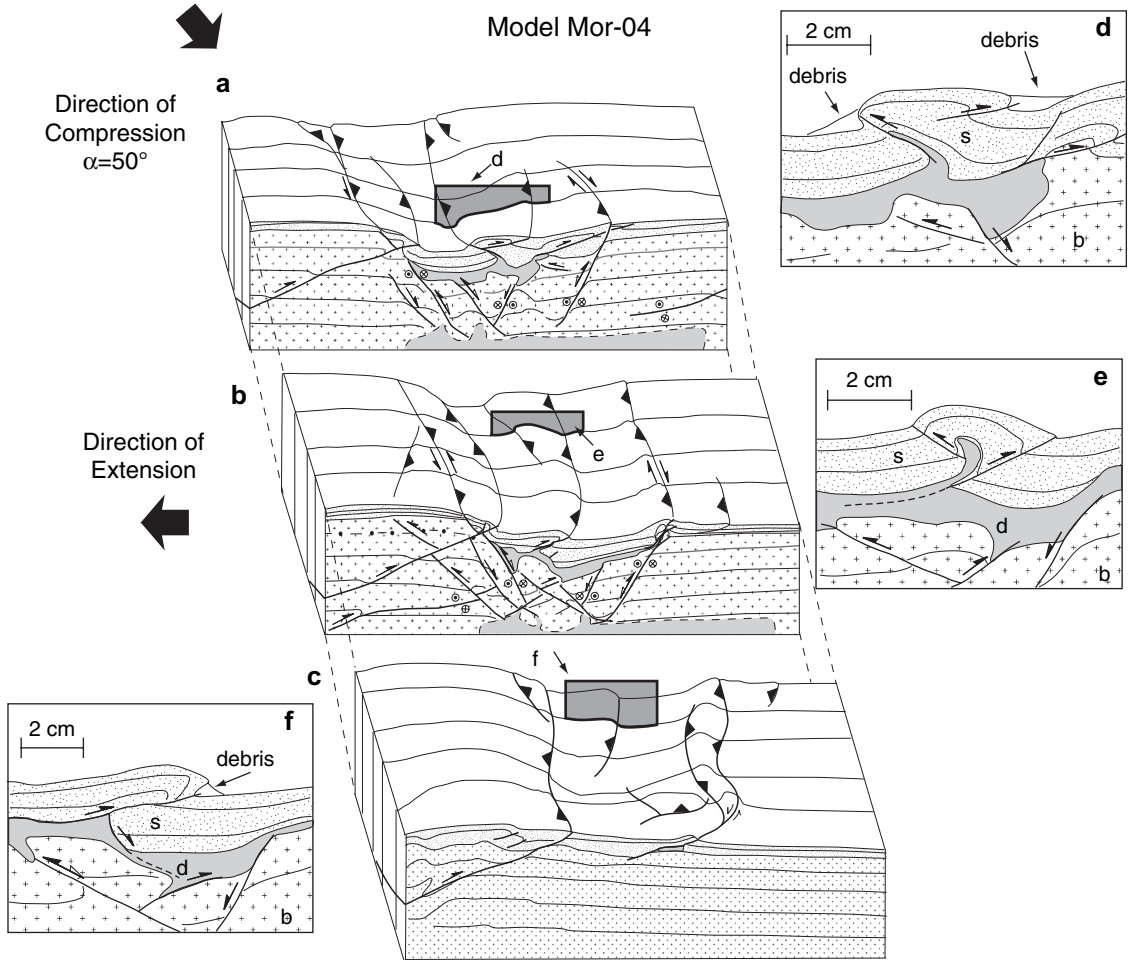

Fig. 9. Three schematic block-diagrams showing the 3D deformational pattern of model Mor-04 ($\alpha = 50°$). (d–f) close-up of the sections showing the main characteristics of the model.

behaviours for high and low obliquity angles. For $\alpha < 40°$, the reduction of graben width with α is clear but not pronounced, whereas for $\alpha \geq 40°$ graben width markedly decreases with α (Fig. 12a). As expected, the graben width decreases with increasing the component of shortening orthogonal to the graben axis. The critical value $\alpha = 40°$ broadly corresponds to the upper limit for fault reactivation observed in previous analogue models (e.g. Brun and Nalpas, 1996).

3.3.3. Horizontal displacement vectors and velocity field

Horizontal displacement vectors have been reconstructed for models with $\alpha = 0°$, 50° and 70° to study the control that pre-existing structures and associated rheological discontinuities may exert on strain field trajectories (Fig. 13). Displacement vectors have been estimated considering the displacement of the passive grid marker nodes in three main steps: (1) the initial position (at the beginning of shortening), (2) after 4 h, and (3) at the end of deformation. Displacement vectors represent the average horizontal velocity of different points onto the model surface and reflect the time-space activity of structures. Surface displacement vectors show how, depending upon the strong decoupling between basin fill and model basement, surface deformation is partitioned in relation to the obliquity angle α.

For model Mor-09 ($\alpha = 0°$), after 4 h of shortening the strain field is characterized by a quite regular pattern with displacement vectors trending mostly parallel to the direction of compression ($v_m \approx 0.5–0.8$ cm h^{-1}, Fig. 13a). Whereas in the proximal part of the model displacement vectors are higher on the shoulders than within the graben, in the distal part the displacement vectors in the graben are higher ($v_m \approx 0.37$ cm h^{-1}) than on the shoulders ($v_m \approx 0.15$ cm h^{-1}; Fig. 13a). This behaviour can be related to a transfer of deformation towards the external sectors via the silicone at the base of the graben fill. At the end of deformation, the horizontal displacement vectors along the border faults trend about 15–20° to the direction of the maximum stress axis, probably due to the reactivation of these faults as tear-faults by the activation of the main thrust (Fig. 13b). In the most external sector, the difference in velocity between the graben and the shoulders ($v_m = 0.22$ cm h^{-1} vs. $v_m = 0.03$ cm h^{-1}) is even more pronounced, still evidencing the great decoupling provided by the syn-rift silicone.

In model Mor-04 ($\alpha = 50°$), after 4 h of shortening, the horizontal displacement vectors deflect towards the central sector

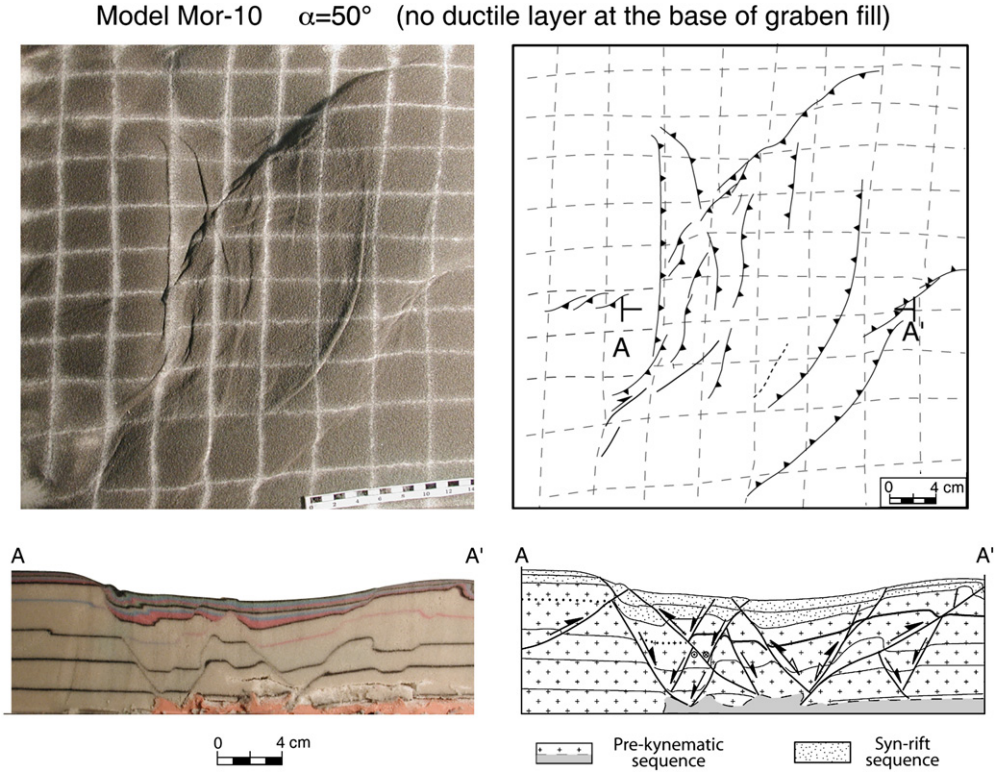

Fig. 10. (a) Top view photo and line drawing at the end of the shortening phase of model Mor-10 ($\alpha = 50°$) performed without syn.-rift silicone layer; (b) longitudinal cross-sections and line drawing (location in a).

of the model of about 30°, showing in the central part of the graben an orientation at high angle to the direction of compression (Fig. 13c). The average velocity vectors decrease quite linearly up to the new-forming structures within the graben fill, where there is a strong reduction in magnitude (v_m is less than 0.1 cm h^{-1}). At the end of deformation the horizontal displacement vectors in the inner part of the model are mostly aligned along with the direction of compression, while in the central and external parts they show a strong deflection (sometime higher than 30°), reflecting a tendency to parallel the graben axis (Fig. 13d). This deflection may be due to a local reorientation of the stress field, which gives rise to strain partitioning partly accommodated by the strike-slip reactivation of basement faults highlighted by the change in CLM colours (Fig. 5).

The velocity field of model Mor-06 ($\alpha = 70°$), after 4 h of deformation, can be sub-divided into two main sectors (Fig. 13e). The first corresponds to the most internal and the upper part of the model, where the horizontal displacement vectors are oriented about 20° to the direction of compression and their magnitude roughly diminishes broadly linearly away from the moving wall. The second sector corresponds to the distal part of the model and it is characterized by a strong decrease in vectors magnitude (v_m changes from ≈ 0.4 cm h^{-1} to ≈ 0.1 cm h^{-1}). The boundary between these two sectors can be identified in correspondence of a new-forming diapiric structure, which is in turn triggered by the dip-slip reactivation of an underlain basement faults (Del Ventisette et al., 2005). At the end of shortening (Fig. 13f), the development of the diapiric structure in the central part of the model is highlighted by the lowest horizontal displacement vectors, which probably reflect the prevalent vertical uplift localized on this structure.

The horizontal displacement vectors of model Mor-10 (deformed with $\alpha = 50°$ but without the silicone layer at the base of the graben fill), gives useful hints about the role of décollement layers on strain propagation (Fig. 13g–h). After 4 h of shortening as well as at the end of deformation, the mean displacement vectors display orientation quite aligned along with the direction of shortening in all sectors of the model, whereas the intensity of the horizontal displacement vectors decrease broadly linearly with increasing distance from the moving wall. This indicates that the early normal faults do not seem to play here any important role on local stress reorientation (at least at surface) as happens instead in the correspondent model incorporating the syn-rift ductile layer (compare Fig. 13c–d with Fig. 13g–h). This different trend in the horizontal displacement vectors indicates not only that the syn-rift ductile layer creates a strongly decoupling between the basement and the sedimentary cover, but also suggests that the lateral rheological discontinuities (ductile vs. brittle rheology) along the graben boundaries are responsible for the local stress reorientations.

4. Conclusive remarks

Analogue modelling has been used to investigate the modalities of graben inversion with particular attention to the role played by the angle (α) between the horizontal direction of shortening and the strike of pre-existing extensional

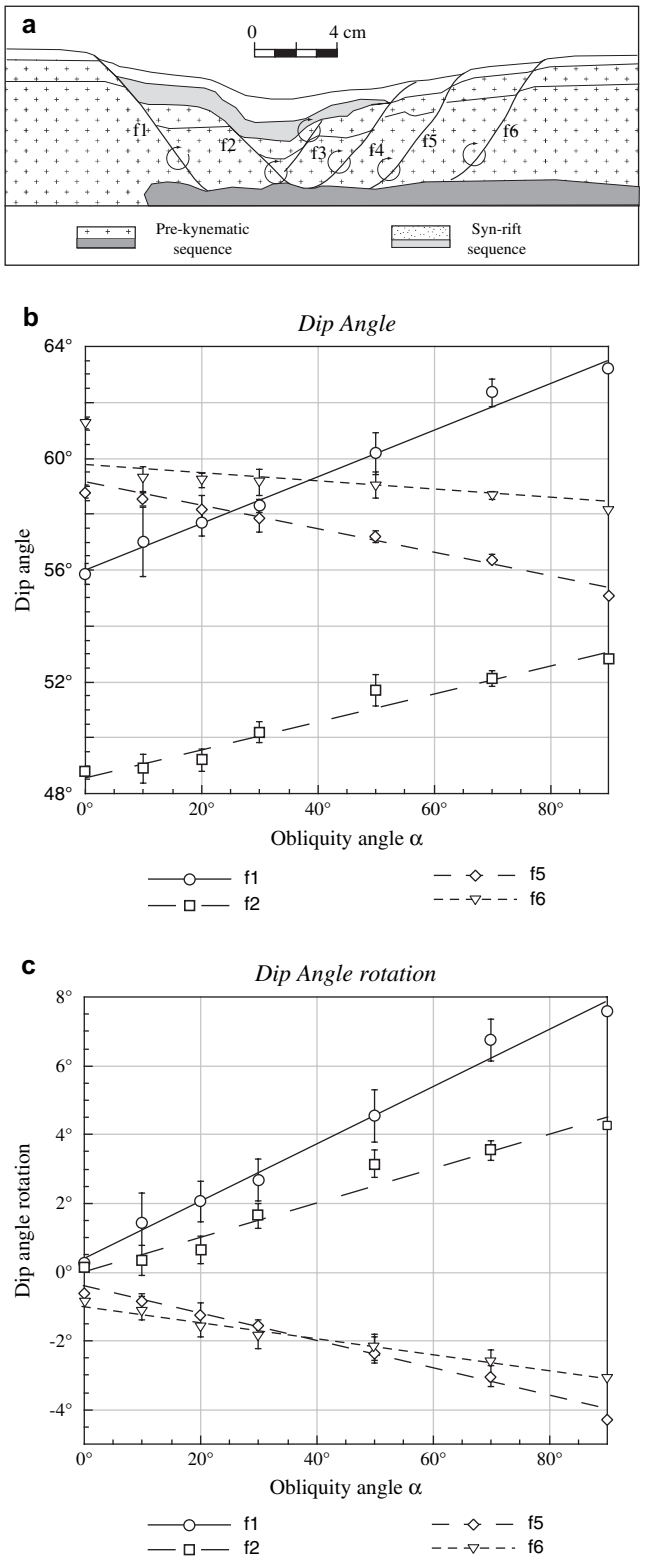

Fig. 11. (a) Schematic cross-section line drawing of model Mor-00 in which are indicated the main faults developed at the end of the extensional phase. For the calculation of the dip angle we used faults f_1, f_2, f_5 and f_6. Average dip angles of faults prior to compression are as follows: $f_1 = 55° \pm 0.6$; $f_2 = 48.5° \pm 0.3$; $f_5 = 59° \pm 0.6$; $f_6 = 61° \pm 0.7$. (b) Diagram showing the dip angle in the various models at the end of the shortening phase for the faults listed above. (c) Diagram showing the values of dip angle rotation compared with the dip angle of the same faults measured at the end of the extensional phase.

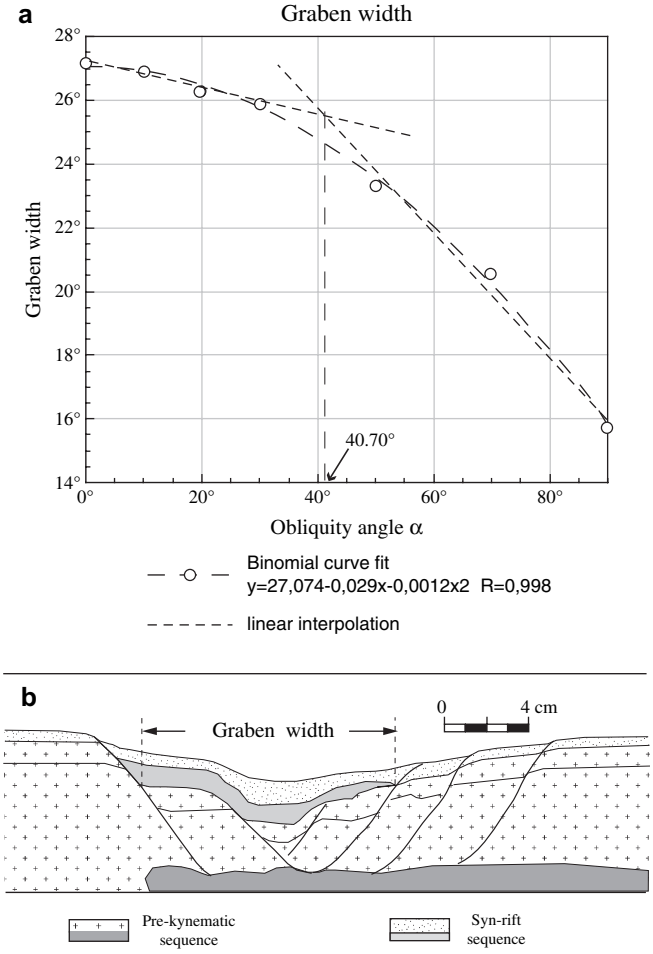

Fig. 12. (a) Graph showing the variation of graben width in relation to the obliquity angle α. (b) Schematic line drawing cross-section of model Mor-00 (deformed only in extension) in which is indicated the graben width at the base of the syn-rift silicone layer.

structures bounding a graben. Despite some parameters have not been taken into account, such as erosion, the influence of fluid pressure on faulting and temperature variation during the deformation as well as minor rheological discontinuities in ductile and brittle layers, the results of this experimental study provided useful indication about tectonic processes characterising basin inversion and fault reactivation. These results are expected to provide useful hints for deciphering the complex evolution of structures characterising many natural cases. The experiments described in this paper suggest the following main conclusions:

(1) deformation during shortening is strongly influenced by previous extensional structures and by the associated rheological discontinuities. The compressive strain is initially accommodated by the reactivation of pre-existing structures and the major rheological discontinuities, and only successively newly-formed structures develop sub-perpendicular to the direction of shortening.
(2) in all the models, the major extensional faults were invariably reactivated during the compressive phase whatever the angle α. This behaviour partly differs from previous

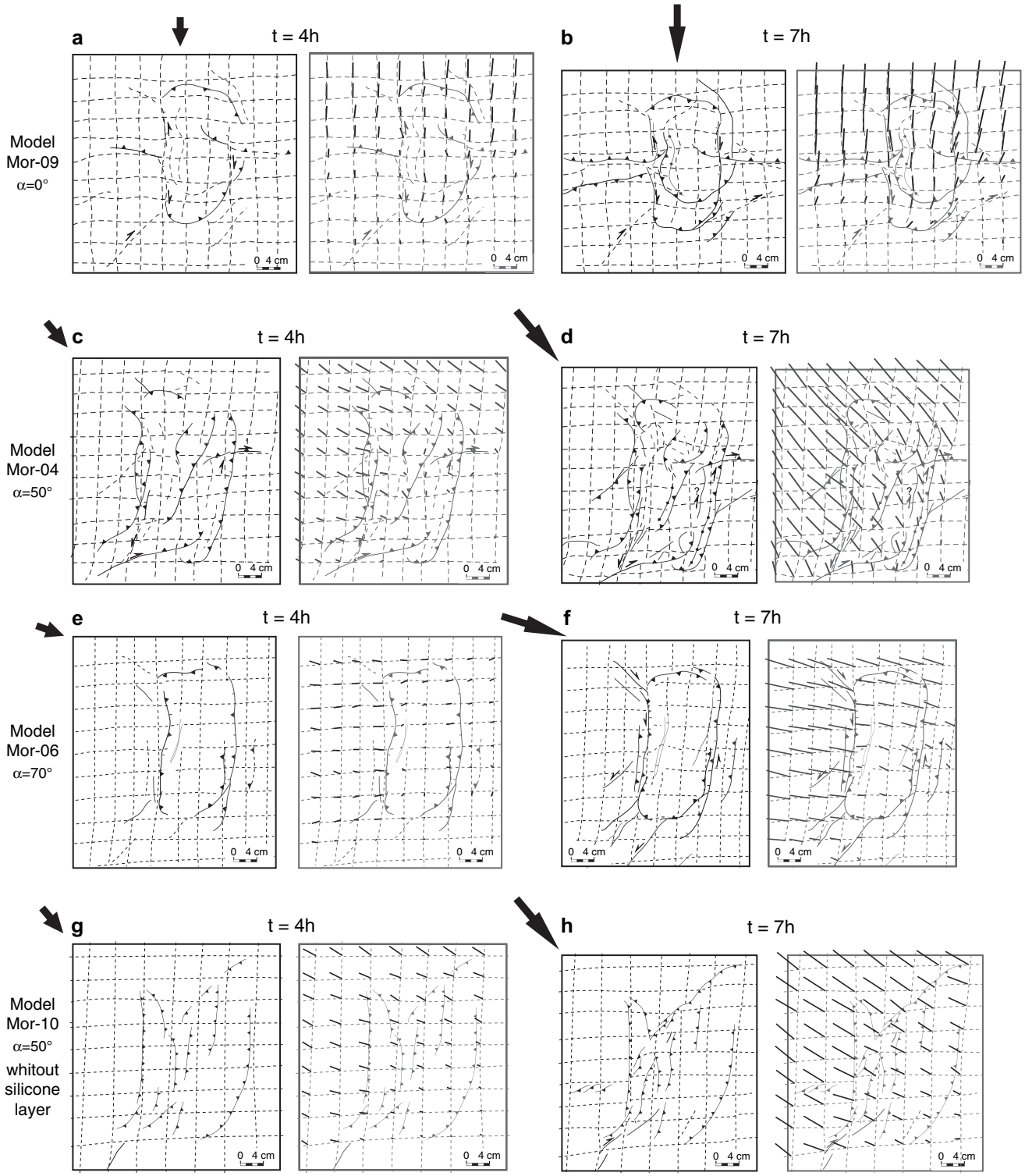

Fig. 13. Horizontal displacement vectors after 4 h of shortening and at the end of deformation (7 h). The vectors are estimated by the different position of some points of the passive grid drawn onto the models surface. (a–b) model Mor-09 ($a = 0°$); (c–d) model Mor-04 ($\alpha = 50°$); (e–f) model Mor-06 ($\alpha = 70°$); (g–h) model Mor-10 ($\alpha = 50°$).

analogue studies in which normal faults were generally reactivated up to $\alpha \leq 45°$. Reactivation of faults under any angle α in the current series of models probably depends upon the model set-up, which did not include any rigid basal VD. On this basis, we argue that the stress components on the fault planes influence fault reactivation and fault rotation in relation to α.

(3) the results of the current experimental series indicate that the main differences among the models concern the timing of deformation and the relative components of reactivation

(strike-slip or dip-slip). For low obliquity angles ($\alpha < 40°$), pre-existing structures act prevalently as dislocation zones and tear-faults for newly-formed thrusts. For high obliquity angles ($\alpha \geq 40°$), the strain is instead mostly accommodated by reactivation of pre-existing structures. Obviously, the principal component of inversion is proportional to the obliquity angles α, so that the qualitative ratio between strike-slip to dip-slip components decreases with increasing α. Minor strike-slip components affect basement faults for very high obliquity angles (for example $\alpha = 70°$, but not for $\alpha = 90°$) probably because of the local reorientation of the stress field nearby these structures.

(4) model deformation is invariably accompanied by dip rotation of major fault planes (except for $\alpha = 0°$), showing a linear relation with the obliquity angle α. This may indicate a reorientation of the pre-existing structures before their reactivation. Similarly, a reduction in graben width accompanied basin shortening. Such a variation in graben exhibits two distinct behaviours for high- and low obliquity angles, with a critical value around $\alpha = 40°$.

(5) the horizontal displacement vectors give quantitative indications on the influence of pre-existing structures and rheological discontinuities on strain partitioning and final deformational patterns. Particularly, the presence of a shallow décollement at the base of the graben strongly modifies the deformational pattern in the sedimentary cover by creating a strong decoupling between the basement and the syn-rift succession. Displacement vectors highlight that the lateral rheological discontinuities between the ductile base of the graben fill and the brittle basement are able to create relevant local reorientations in the stress field.

(6) for high obliquity angles ($\alpha = 50°$, $70°$ and $90°$), a diapiric structure formed above a major fault in the graben axial zone. Such a structure would be mostly due to the high dip-slip component of reactivation along this fault, injecting the silicone putty along the fault plane and then into the core of the diapiric structure (for details, see Del Ventisette et al., 2005).

Acknowledgments

We thank Prof. H. Koyi and Prof. F. Storti for the constructive revisions which helped to improve the manuscript. We also thank Dr Giovanna Moratti and Dr Giacomo Corti for inspiring discussion and helpful suggestions. Dr Baldi of the Colorobbia Italia S.p.A. is thanked for providing the quartz-sand used in our experiments. This work was funded by the Department of Earth Science of University of Florence and CNR-IGG (Florence Section).

Appendix A. Scaling of the models

Scaling of analogue models to the natural prototype require the geometrical, rheological, kinematical and dynamical similarities to be satisfied (e.g. Hubbert, 1937; Ramberg, 1981; Weijermars and Schmeling, 1986; Table 2). To investigate in detail the models deformation patterns the models were suitably scaled such that 1 cm in the model represents 1 km in nature, involving a geometrical length ratio $l^* = l_{mod}/l_{nat} = 10^{-5}$.

Following Hubbert (1937) and Ramberg (1981), the stress σ^* acting on the model is given by the relation:

$$\sigma^* = \frac{\sigma_{mod}}{\sigma_{nat}} = \rho^* g^* l^* = \frac{\rho_{mod}}{\rho_{nat}} \frac{g_{mod}}{g_{nat}} \frac{l_{mod}}{l_{nat}}. \quad (1)$$

Considering the length ratio $l^* = 10^{-5}$, $g^* = 1$ and $\rho^* = 0.48$ (using a natural salt density of 2200 kg/m^3), the stress ratio $\sigma^* \approx 4.8 \times 10^{-6}$ Pa (see Table 2).

The brittle behaviour of rocks can be expressed by the Mohr–Coulomb criterion of failure:

$$\tau_b = \mu\sigma_N(1 - \lambda) + c, \quad (2)$$

where τ_b and σ_N are the shear and normal stress on the fault plane, λ is the Hubbert–Rubey coefficient of fluid pressure, c is the cohesion and μ is the internal friction coefficient expressed as:

$$\mu = \tan\phi, \quad (3)$$

where ϕ is the angle of internal friction. Because of in our models $\lambda = 0$ the Mohr–Coulomb criterion of failure can be rewriting as:

$$\tau_b = \sigma_N \tan\phi + c. \quad (4)$$

Since cohesion has stress dimension, it must share a similar scaling ratio:

$$c^* = c_{mod}/c_{nat} = \sigma^*. \quad (5)$$

In the same way the internal friction coefficient – expressed by Eq. (4) – must have similar values both in models and in nature. The Newtonian behaviour is expressed by the linear relationship between stress and strain of the Newton equation:

$$\tau_d = \eta\left(\frac{v}{H_d}\right) = \eta\gamma_d, \quad (6)$$

where τ_d is the deviatoric shear stress on the viscous layer, η is the dynamic viscosity, and γ_d is the engineering shear strain. The time ratio can be then computed from equation:

$$t^* = \frac{t_{mod}}{t_{nat}} = \frac{1}{\varepsilon^*} = \frac{H_d\varepsilon_{nat}}{v_{mod}}, \quad (7a)$$

where H_d is the thickness of the ductile layer. Rewriting this equation as a function of time:

$$t_{nat} = \frac{t_{mod} v_{mod}}{H_d \varepsilon_{nat}}. \quad (7b)$$

The rate of syn-tectonic sedimentation can be calculated considering the length and the time ratios (Table 2). From relation (7b), shortening and sedimentation rates scale to 2.5 mm/y^{-1}

and 0.58 mm/y^{-1}, respectively (Table 2), which are in good agreement with values normally observed in nature.

References

Allemand, P., Brun, J.P., Davy, P., Van Den Driessche, J., 1989. Symètrie et asymétrie des rifts et mécanismes d'amincissement de la lithosphere. Bulletin de la Société Géologique de France 3, 445–451.

Bouatmani, R., Medina, F., Ait salem, A., Hoepffner, C., 2003. Thin-skin tectonics in the Essaouira basin (western High Atlas, Morocco): evidence from seismic interpretation and modelling. Journal of African Earth Sciences 37, 25–34.

Brace, W.F., Kohlmmstedt, D.L., 1980. Limits on lithospheric stress imposed by laboratory experiments. Journal of Geophysical Research 85, 6248–6252.

Brun, J.P., Nalpas, T., 1996. Graben inversion in nature and experiments. Tectonics 15, 677–687.

Buchanam, P.G., McClay, K.R., 1991. Sandbox experiments of inverted listric and planar fault systems. In: Cobbold, P.R. (Ed.), Experimental and Numerical Modelling of Continental Deformation. Tectonophysics 188, pp. 97–115.

Buiter, S.J.H., Pfiffner, O.A., 2003. Numerical models of the inversion of half-graben basins. Tectonics 22, doi:10.1029/2002TC001417.

Byerlee, J.D., 1978. Friction of rocks. Pure and Applied Geophysics 116, 615–626.

Del Ventisette, C., Montanari, D., Bonini, M., Sani, F., 2005. Positive fault inversion triggering ''intrusive diapirism'': an analogue modelling perspective. Terra Nova 17, 478–485, doi:10.1111/j.1365-3121.2005.00637.x.

Dubois, A., Odonne, F., Massonnat, G., Lebourg, T., Fabre, R., 2002. Analogue modelling of fault reactivation: tectonic inversion and oblique remobilisation of grabens. Journal of Structural Geology 24, 1741–1752.

Faccenna, C., Nalpas, T., Brun, J.P., Davy, P., 1995. The influence of pre-existing thrust faults on normal fault geometry in nature and experiments. Journal of Structural Geology 17, 1139–1149.

Faugères, J.C., 1978. Les rides sud-rifaines. Evolution sedimentaire et structurale d'un bassin atlantico-mésogéen de la marge africaine. Ph.D. thesis, University of Bordeaux.

Faugères, J.C., 1981. Évolution structurale d'un bassin atlantico-mésogéen de la marge africaine: les rides sud-rifaines (Maroc). Bulletin de la Société Géologique de France 23, 229–244.

Gartrell, A., Hudson, C., Evans, B., 2005. The influence of basement faults during extension and oblique inversion of the Makassar Straits rift system: insights from analog models. AAPG Bulletin 89 (4), 495–506, doi:10.1306/12010404018.

Hafid, M., 2000. Triassic-early Liassic extensional systems and their Tertiary inversion, Essaouira Basin (Morocco). Marine and Petroleum Geology 17, 409–429.

Hafid, M., Ait Salem, A., Bally, A.W., 2000. The western termination of the Jebilet-High Atlas system (Offshore Essaouira Basin, Morocco). Marine and Petroleum Geology 17, 431–443.

Hansen, D.L., Nielsen, S.B., 2003. Why rifts invert in compression. Tectonophysics 373, 5–24.

Higgins, R.I., Harris, L.B., 1997. The effect of cover composition on extensional faulting above re-activated basement faults. Results from analogue modelling. Journal of Structural Geology 19, 89–98.

Hubbert, M.K., 1937. Theory of scale models as applied to the study of geologic structures. Geological Society of America Bulletin 48, 1459–1520.

Koopman, A., Speksnijder, A., Horsfield, W.T., 1987. Sandbox model studies of inversion tectonics. Tectonophysics 137, 379–388.

Krantz, R.W., 1991. Measurements of friction coefficients and cohesion for faulting and fault reactivation in laboratory models using sand and sand mixtures. Tectonophysics 188, 203–207.

Letouzey, J., Colletta, B., Vially, R., Chermette, J.C., 1995. Evolution of salt-related structures in compressional settings. In: Jackson, M.P.A., Roberts, D.,G., Snelson, S. (Eds.), Salt Tectonics: A Global Perspective. American Association of Petroleum Geologists Memoir 68, 41–60.

Mandl, G., 1988. Mechanics of tectonic faulting – models and basic concepts. In: Zwart, H.J. (Ed.), Development in Structural Geology 1. Elsevier.

Mandal, N., Chattopadhyay, A., 1995. Modes of reverse reactivation of domino-type normal faults: experimental and theoretical approach. Journal of Structural Geology 17, 1151–1163.

McClay, K.R., 1989. Analogue models of inversion tectonics. In: Cooper, M.A., Williams, G.D. (Eds.), Inversion Tectonics. Geological Society, London, Special Publication 44, pp. 41–62.

McClay, K.R., Buchanam, P.G., 1992. Thrust faults in inverted extensional basin. In: McClay, K.R. (Ed.), Thrust Tectonics. Chapman and Hall, London, pp. 93–104.

Mitra, S., Islam, Q.T., 1994. Experimental (clay) models of inversion structures. Tectonophysics 230, 211–222.

Nalpas, T., Brun, J.P., 1993. Salt flow and diapirism related to extension at crustal scale. Tectonophysics 228, 349–362.

Nalpas, T., Le Douran, S., Brun, J.P., Untrnehr, P., Richert, J.P., 1995. Inversion of the Broad Fourteens Basin (offshore Netherlands), a small-scale model investigation. Sedimentary Geology 95, 237–250.

Panien, M., Schreus, G., Pfiffner, A.O., 2005. Sandbox experiments on basin inversion: testing the influence of basin orientation and basin fill. Journal of Structural Geology 27, 433–445.

Piqué, A., Le Roy, P., Amrhar, M., 1998. Transtensive synsedimentary tectonics associated with ocean opening: the Essaouira–Agadir segment of the Atlantic margin. Journal of Geological Society of London 155, 913–928.

Ramberg, H., 1981. Gravity, Deformation and the Earth's Crust in Theory, Experiments and Geologic Application, second ed. Academic Press, London, 452 pp.

Ranalli, G., Yin, Z.M., 1990. Critical stress difference and orientation of fault in rocks with strength anisotropies: the two-dimensional case. Journal of Structural geology 12, 1067–1071.

Richard, P., 1989. Experiments on reactivation of normal faults in a sedimentary cover overlying a reactivated basement fault. Fifth meeting of the European Union of Geosciences, Strasbourg, Terra Abstr, 1(1), 72.

Richard, P., Krantz, R.W., 1991. Experiments on fault reactivation in strike-slip mode. Tectonophysics 188, 117–131.

Sandiford, M., 1999. Mechanics of basin inversion. Tectonophysics 305, 109–120.

Sassi, W., Colletta, B., Balé, P., Paquereau, T., 1993. Modelling of structural complexity in sedimentary basins: the role of pre-existing faults in thrust tectonics. Tectonophysics 226, 97–112.

Sibson, R.H., 1985. A note on fault reactivation. Journal of Structural Geology 7, 751–754.

Tron, V., Brun, J.P., 1991. Experiments on oblique rifting in brittle–ductile systems. Tectonophysics 188, 71–84.

Weijermars, R., Schmeling, H., 1986. Scaling of Newtonian and non-Newtonian fluid dynamics without inertia for quantitative modelling of rock flow due to gravity (including the concept of rheological similarity). Physics of the Earth and Planetary Interiors 43, 316–330.

Yamada, Y., McClay, K., 2003a. Application of geometric models to inverted listric fault systems in sandbox experiments. Paper 1: 2D hanging-wall deformation and section restoration. Journal of Structural Geology.

Yamada, Y., McClay, K., 2003b. Application of geometric models to inverted listric fault systems in sandbox experiments. Paper 2: insights for possible along strike migration of material during 3D hanging-wall deformation. Journal of Structural Geology 25, 1–6.

Yin, Z.M., Ranalli, G., 1992. Critical stress difference, fault orientation and slip direction in anisotropic rocks under non-Andersonian stress systems. Journal of Structural Geology 14, 237–244.

Zizi, M., 1996a. Triassic–Jurassic Extensional System and their Neogene Reactivation in Northern Morocco (the Rides prerifaines and Guercif Basin). Ph.D. thesis, Rice University, Houston, 229.

Zizi, M., 1996b. Triassic–Jurassic extension and Alpine inversion in the northern Morocco. In: Ziegler, P.A., Horvath, F. (Eds.), Peri-Tethys Memoir 2: Structure and Prospects of the Alpine Basins and Forelands. Mem. Mus. Natn. Hist. Nat. 170, 87–101.